CrossMark
click for updates

On the synthesis and characterisation of luminescent hybrid particles: Mo$_6$ metal cluster complex/SiO$_2$†

Yuri A. Vorotnikov,[ab] Olga A. Efremova,*[c] Natalya A. Vorotnikova,[ab] Konstantin A. Brylev,[abd] Mariya V. Edeleva,[be] Alphiya R. Tsygankova,[ad] Anton I. Smolentsev,[ad] Noboru Kitamura,[f] Yuri V. Mironov[ad] and Michael A. Shestopalov*[abd]

Photoluminescent silica-based materials are used in applications in photonics, sensing, and biological and medical sciences. Specifically, hybrid particles based on silica doped by photoluminescent octahedral molybdenum metal cluster complexes are inexpensive and readily available *via* the Stöber process and thus are promising materials for diverse applications. We evaluated design of photoluminescent materials based on silica and $\{Mo_6X_8\}^{4+}$ clusters (where X = Cl, Br, I), including how synthesis conditions (chemical composition of metal cluster precursors $(Bu_4N)_2[\{Mo_6X_8\}(NO_3)_6]$, loading of the precursor and presence of a surfactant) influence key parameters of the final materials, such as phase composition, size and morphology of the particles and photophysical characteristics. Our study revealed that hydrolysis of the molybdenum cluster precursors during the Stöber process strongly affects both morphology and photophysical parameters of the materials, especially at high loadings. At relatively low loadings of the precursors, materials doped by $\{Mo_6I_8\}^{4+}$ clusters demonstrated the most promising set of properties— the highest photoluminescence quantum yields and efficient singlet oxygen generation—while particle size and morphology remained the same as for undoped SiO_2 materials.

1. Introduction

Hexanuclear molybdenum cluster complexes with the general formula $[\{Mo_6X_8\}L_6]$ (X = Cl, Br, or I; L = apical organic or inorganic ligands) (Fig. 1) offer an outstanding balance of photophysical and chemical properties that make them highly promising for applications in biomedical, sensing and optical technologies.[1] These complexes demonstrate high chemical- and photo-stability of the cluster core $\{Mo_6X_8\}^{4+}$ that are primarily responsible for their triplet excited-state photoluminescence (*i.e.*, phosphorescence) with broad emission spectra extending in the red/near infra-red region (from ~550 to >950 nm).[2–10] The complexes are characterised by impressive photoluminescence quantum yields (PLQYs) for coordination compounds[2,6] and can also act as powerful photosensitisers in generating singlet oxygen ($^1O_2$).[6–9,11–14] Importantly, the photophysical properties of molybdenum metal cluster complexes are strongly dependent on the chemical environment of the cluster Mo$_6$, that is, inner ligands X and apical ligands L.

For any of the above applications, however, the molybdenum cluster complexes must be supported by a bespoke matrix. For
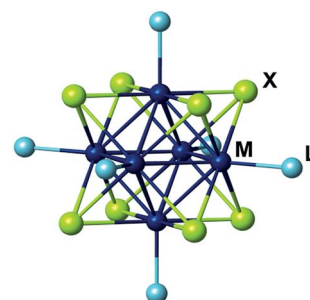
[a]Nikolaev Institute of Inorganic Chemistry SB RAS, 3 Acad. Lavrentiev Ave., 630090 Novosibirsk, Russian Federation. E-mail: shtopy@niic.nsc.ru; Fax: +7-383-330-94-89; Tel: +7-383-330-92-53

[b]Scientific Institute of Clinical and Experimental Lymphology, 2 Timakova St., 630060 Novosibirsk, Russian Federation

[c]Department of Chemistry, University of Hull, Cottingham Road, Hull, HU6 7RX, UK. E-mail: o.efremova@hull.ac.uk; Tel: +44 (0)1482 465417

[d]Novosibirsk State University, 2 Pirogova st., 630090 Novosibirsk, Russian Federation

[e]Novosibirsk Institute of Organic Chemistry SB RAS, 9 Acad. Lavrentiev ave., 630090 Novosibirsk, Russian Federation

[f]Department of Chemistry, Faculty of Science, Hokkaido University, 060-0810 Sapporo, Japan

† Electronic supplementary information (ESI) available: Experimental section, CIF files with crystallographic data (CSD-429897; CSD-429898); figures, tables, FTIR, UV/Vis diffuse reflectance, ^{1}H NMR and photoemission spectra, TEM, SEM and confocal laser scanning microscopy images, TG and DTG curves. See DOI: 10.1039/c6ra04321f

Fig. 1 Representation of $[\{Mo_6X_8\}L_6]$ cluster complex.

example, to target biological applications, the matrix should offer biocompatibility, while for optical applications the matrix should be transparent.[5,15–20] Silica is considered a universal matrix, as it can be used to target both biological[21–25] and materials-based applications.[26–29] Indeed, silica itself is a cheap, optically transparent, non-toxic and versatile material. It can be prepared with high specific surface area or be obtained in the form of nano/microparticles, surfaces or bulk.

In recent decades, several research efforts were devoted to synthesis of silica nanoparticles (SNPs), doped by molybdenum cluster compounds, such as $Cs_2[\{Mo_6X_8\}X_6]$ (X = Cl, Br, I)[30] and $(Bu_4N)_2[\{Mo_6I_8\}(CF_3COO)_6]$[6] to target biological[31] and optical applications.[32] To incorporate hexamolybdenum cluster complexes into silica nanoparticles, they were added to a reaction mixture during the Stöber process (i.e., hydrolysis of tetraethoxysilane [TEOS] by ammonia solution) in a stabilised water-in-oil emulsion. Notably, Aubert et al. reported that apical ligands of $[\{Mo_6Br_8\}Br_6]^{2-}$ were substituted during the hydrolysis of TEOS by either silanol (Si–O$^-$) or hydroxo ligands.[31] Despite the observed ability of molybdenum metal clusters, no studies were undertaken to establish (1) effects that ligand substitution or hydrolysis of the molybdenum cluster complexes during the Stöber process have on optical properties of the final material, especially photoluminescence quantum yields; (2) the highest loading of molybdenum metal cluster possible in SiO_2; (3) how particle morphology is affected by doping with molybdenum cluster complexes; and (4) how particle size influences particle photophysical properties.

To answer these questions, we investigated in detail properties of silica microparticles (SMPs) that are realised when TEOS is hydrolysed by ammonia solution (Stöber process) in the presence of various quantities of molybdenum cluster complexes $(Bu_4N)_2[\{Mo_6X_8\}(NO_3)_6]$ (where X is Cl (1), Br (2), or I (3)). 1–3 were selected due to the recognised ability of NO_3^- ligands to be easily substituted by other ligands, which likely results in covalent bonding between the molybdenum cluster core $\{Mo_6X_8\}^{4+}$ and silica matrix. Specifically, we investigated morphology, structure, optical and physical properties of resultant materials using X-ray powder diffraction, electron microscopy techniques (including elemental mapping), photoluminescence spectroscopy, and elemental analysis. Finally, to assess the influence of particle size, we compared photophysical properties and singlet oxygen generation activity of SMPs with those of corresponding silica nanoparticles (SNPs), obtained via the Stöber process in water-in-oil emulsion.

2. Experimental section

2.1 Synthesis section

All reagents and solvents employed were commercially available and used as received without further purification. $(Bu_4N)_2$-$[\{Mo_6X_8\}(NO_3)_6]$, where X = Cl (1), Br (2), I (3), were prepared according to the described procedures.[5,33]

2.1.1 Stöber method for preparation of n^x@SiO_2 SMPs. The general procedure for synthesis of n^x@SiO_2 (500 nm), where **n** is the initial complex 1, 2 or 3 and x is the loading of **n** in grams per 1 g of obtained SiO_2 equal to 0.0001, 0.001, 0.005, 0.01, 0.05,

0.1, 0.5, 1, 2, 3, 4, or 5, follows: 6 mL of acetone solution containing the cluster complex **n** (0.0135, 0.135, 0.675, 1.35, 6.75, 13.5, 67.5, 135, 270, 405, 540 or 675 mg) were placed in a 10 mL vial. TEOS (0.5 mL), H_2O (0.75 mL) and 25% aqueous ammonia solution (0.5 mL) were added to the vial, while stirring vigorously. The vials were capped and stirred for 12 h at room temperature. The obtained solutions, which had colors ranging from yellow to red depending on the content of **n**, were centrifuged (7000 rpm for 10 min), washed by several sonication/centrifugation cycles: 5 times with acetone and 5 times with water and finally dried at 60 °C in air.

2.1.2 Water-in-oil microemulsion method for preparation of 3^x@SiO_2 SNPs. The general procedure for synthesizing 3^x@SiO_2, where x = 0, 0.001, 0.005, 0.01, 0.05, 0.1 (~50 nm) by W/O microemulsion, follows: compound 3 (0, 1.7, 8.5, 17, 85 or 170 mg) was dissolved in ethanol (2.5 mL). Distilled water (2.5 mL) was then added to the obtained ethanol solution of 3. In a separate 250 mL-flask, Brij L4 surfactant (15 mL) was dissolved in n-heptane (47 mL). To prepare the microemulsion, the ethanol/water solution of 3 (1.6 mL) and 25% aqueous ammonia solution (1.3 mL) were separately added to the flask with the surfactant oil solution. This mixture was stirred for 30 min to ensure homogeneity of the microemulsion. Next, 2 mL of TEOS was added, and the solution stirred for 3 days. Thereafter, the obtained yellowish solution was centrifuged (7000 rpm for 10 min), washed by several sonication/centrifugation cycles: 3 times with ethanol, 2 times with water and 1 time with acetone and then dried at 60 °C in air.

2.1.3 Preparation of precipitates An and Bn. Precipitates **An** and **Bn** where **n** refers to compounds 1, 2 or 3, were obtained in separate batches in the following procedures: 500 mg of **n** (0.291 mmol of 1, 0.241 mmol of 2, or 0.204 mmol of 3) were dissolved in acetone (30 mL). Next, 2.5% aqueous ammonia solution (3.2 mL) was added. The immediate precipitation of an orange solid was observed. Precipitate **An** was filtered after 12 h. Precipitate **Bn** was collected after complete evaporation of the mother liquor in air. All precipitates were washed 3 times by acetone and air dried. In precipitates **B2** and **B3**, crystals suitable for single-crystal X-ray analysis were found. Yields calculated for the product of formula $[\{Mo_6X_8\}(H_2O)_2(OH)_4]\cdot 2H_2O$ were 278 mg (95.5%), 319 mg (97.6%) and 298 mg (84.3%) for X = Cl ($4\cdot 2H_2O$), Br ($5\cdot 2H_2O$) and I ($6\cdot 2H_2O$), respectively. Yield calculated for $5\cdot 6H_2O$ was 323 mg (93.9%).

2.2 Analytical methods

The size and morphology of the n^x@SiO_2 micro- and nanoparticles were characterized by scanning electron microscopy (SEM) using a JEOL JSM-5700 CarryScope microscope and by transmission electron microscopy (TEM) using a Libra 120 (Zeiss) TEM. Elemental maps in SMPs were recorded using the standard three-window technique described in Brydson, Electron Energy Loss Spectroscopy (Bios Scientific Publishers Ltd, 2001). Confocal imaging of SMPs was performed using a Zeiss LSM 780 NLO confocal microscope (Carl Zeiss Inc., Jena, Germany) based on an AxioObserver Z1 (Zeiss) microscope and

equipped with a laser diode (405 nm) for fluorescence and with a APOCHROMAT 63×/1.4 Oil DIC LD Plan objective.

The CHN elemental analyses were performed on a Euro-Vector EA3000 Elemental Analyser. Molybdenum content in samples was determined on a high-resolution spectrometer iCAP-6500 (Thermo Scientific) with a cyclone-type spray chamber and "SeaSpray" nebulizer. The spectra were obtained by axial plasma viewing. Standard operating conditions of the ICP-AES system follow: power = 1150 W, injector inner diameter = 3 mm, carrier argon flow = 0.7 L min^{-1}, accessorial argon flow = 0.5 L min^{-1}, cooling argon flow = 12 L min^{-1}, number of parallel measurements = 3, and integration time = 5 s. Deionized water ($R \approx 18$ MΩ) was used to prepare sample solutions. All chemical reagents were of analytical grade.

^{29}Si CP-MAS solid-state NMR was recorded on the 500 MHz Bruker Advance II. The specific surface area of SMPs and SNPs was measured by a nitrogen cryoadsorption technique using Autosorb iQ (Quantachrome Instruments) at 77 K. The samples were first degassed in vacuum at 393 K overnight. N$_2$ adsorption–desorption isotherms were measured within the range of relative pressures of 10^{-5} to 0.99 and calculated from the data obtained on the basis of the conventional BET model.

2.2.1 Luminescence measurements. Absorbance of acetone solutions of (Bu$_4$N)$_2$[{Mo$_6$X$_8$}(NO$_3$)$_6$] (X = Cl or Br) was set to <0.1 at 355 nm. The solutions were poured into quartz cuvettes and deaerated by purging with argon gas for 30 min. The cuvettes were then sealed. The measurements were carried out at 298 K. The samples were excited by 355 nm laser pulses (6 ns duration, LOTIS TII, LS-2137/3). Corrected emission spectra were recorded on a red-light-sensitive multichannel photodetector (Hamamatsu Photonics, PMA-12). For emission decay measurements, the emission was analyzed by a streakscope system (Hamamatsu Photonics, C4334 and C5094). Emission quantum yields (Φ_{em}) of solutions were estimated by using (Bu$_4$N)$_4$[Re$_6$S$_8$Cl$_6$] as a standard: Φ_{em} = 0.039 in deaerated acetonitrile.

For emission measurements in solid state, powdered samples of compounds **1**, **2** and **3**, **n**^{x}@SiO$_2$ (both SMPs and SNPs) and **An** and **B2** were placed between two non-fluorescent glass plates. The measurements were carried out at 298 K. The samples were excited by 355 nm laser pulses (6 ns duration, LOTIS TII, LS-2137/3). The corrected emission spectra were recorded on a red-light-sensitive multichannel photodetector (Hamamatsu Photonics, PMA-12). For emission decay measurements, the emission was analyzed by a streakscope system (Hamamatsu Photonics, C4334 and C5094). The emission quantum yields were determined by an Absolute Photo-Luminescence Quantum Yield Measurement System (Hamamatsu Photonics, C9920-03), which comprised an excitation Xenon light source (the excitation wavelength was 380 nm), an integrating sphere, and a red-sensitive multichannel photodetector (Hamamatsu Photonics, PMA-12).

2.2.2 Singlet oxygen generation. Singlet oxygen generation was investigated as follows: solution of **n** (2 mg, 0.002 mmol for **1**; 2.5 mg, 0.002 mmol for **2**; 2.8 mg, 0.002 mmol for **3**) or dispersion of 10 mg of **3**^{x}@SiO$_2$ (x = 0.0001, 0.0005, 0.001, 0.002, 0.003, 0.005, 0.01, 0.05, 0.1 for SMPs; and x = 0.001,

0.005, 0.01 for SNPs) and 2,3-diphenyl-*para*-dioxene[34] (28.8 mg, 0.12 mmol) in acetone-d$_6$ (0.6 mL) in a conventional NMR tube was saturated with oxygen for 5 min. The sealed tube was then irradiated by a DRSh-500 mercury lamp with a filtered light ($\lambda \geq$ 400 nm). ^{1}H NMR (200 MHz) spectra were then collected on a Bruker Avance 200 NMR spectrometer.

3. Results and discussion

3.1 Synthesis

A range of molybdenum cluster-doped SMPs, **n**^{x}@SiO$_2$ (where **n** corresponds to complexes **1**, **2**, or **3**; x is a loading of **1**–**3** in g per 1 g of final SiO$_2$), were prepared by hydrolysis of TEOS with a 25% ammonia solution (*i.e.*, by the Stöber process) in the presence of varying amounts of corresponding cluster complexes. Specifically, loadings of the cluster complexes (x) in the reaction mixture ranged from 0.0001 to 5 g per 1 g of resultant SiO$_2$. However, in the case of cluster complex **1**, the loading of the cluster was limited by x = 0.5. This is because **1**^{x}@SiO$_2$ SMPs with $x \geq$ 0.5 had a grayish-blue colour, while the colour of other SMPs ranged from yellow to red solids depending on metal cluster loading.

Several chemical processes and interactions relevant to formation of materials by the Stöber procedure in the presence of **1**–**3** should be considered:

(i) Hydrolysis. Since apical nitrato ligands are well known to be highly labile, it is expected that they can be easily substituted by OH$^-$ or H$_2$O in alkaline aqueous solutions. In other words, alongside the hydrolysis of TEOS, which results in SiO$_2$, a parallel hydrolysis of **1**–**3** is possible with the formation of corresponding aquahydroxo complexes. Indeed, Sheldon showed that the alkalisation of an aqueous solution of [{Mo$_6$X$_8$}X$_6$]$^{2-}$ led to substitution of all apical halogens by OH$^-$ and H$_2$O groups producing precipitates that were described by the general formula [{Mo$_6$X$_8$}(H$_2$O)$_2$(OH)$_4$]·zH$_2$O, where X was Cl (**4**·zH$_2$O), Br (**5**·zH$_2$O), or I (**6**·zH$_2$O).[35,36] He also demonstrated the existence of soluble hexahydroxo complexes [{Mo$_6$X$_8$}-(OH)$_6$]$^{2-}$ in the strongly basic aqueous solutions.[36,37] Similarly, by the reaction of a diluted aqueous solution of (H$_3$O)$_2$[{Mo$_6$Cl$_8$}Cl$_6$]·6H$_2$O with aqueous ammonia, the neutral aquahydroxo complex **4**·12H$_2$O was obtained and its crystal structure was determined by X-ray single-crystal analysis.[38] Additionally, the coexistence of intermediate partially hydrolysed forms was also suggested earlier.[39–41]

(ii) Hydrogen bonding. The formation of hydrolysed molybdenum cluster species, especially aquahydroxo cluster units may suggest that the silica matrix and these cluster species are able to interact by strong hydrogen bonding between silanol (Si–OH) groups and aqua or hydroxo ligands of the cluster complexes.

(iii) Covalent bonding Si–O–Mo. The covalent bonding between the silica matrix and molybdenum cluster complexes was described by Robinson *et al.*[42] and Aubert *et al.*[31] Such interactions can be realised *via* the substitution of apical ligands in cluster complexes by the deprotonated silanol groups (Si–O$^-$), which are formed due to ionisation of Si–OH under basic conditions. Taking into account both hydrogen and

covalent bonding, it is reasonable to express the metal cluster units immobilised in the silica matrix by the general formula $[\{Mo_6X_8\}(H_2O)_{6-y-z}(OH)_y(OSi)_z]^{4-y-z}$. Moreover, with the increased loading of metal clusters, it is likely that z would tend to 0, that is, lead to aqua-hydroxo species.

(iv) Degradation of hexamolybdenum cluster complexes. Sheldon in his earlier work mentioned that Mo(II) in the chloride cluster Mo_6Cl_{12} is sensitive towards oxidation in alkaline solutions giving Mo(V) species.[35] As mentioned above, we also noticed that attempts to prepare 1^x@SiO$_2$ with $x \geq 0.5$ led to formation of a greyish-blue precipitate. This could be explained by destruction of the cluster core as a result of hydrolysis leading to formation of $[\{Mo_6Cl_{8-y}(OH)_y\}(H_2O)_2(OH)_4]$ cluster species[39,40] and their following oxidation to molybdenum blue species (i.e., isopolymolybdates).

To better understand the hydrolysis of **1–3** in an ammonia solution, we simulated the Stöber process conditions, but without TEOS in the reaction mixture. Specifically, we carried out the reactions of acetone solutions of **1–3** with an aqueous ammonia solution. After the reactants were mixed, we observed the quantitative formation of coloured precipitates. For further characterisation, the precipitates were isolated from the reaction mixtures after 12 h (labeled as precipitates **An**), and after the complete evaporation of the solvents in air (labeled as precipitates **Bn**), where **n** relates to **1–3**.

3.2 Materials composition and chemical structure

To establish whether some of the above processes and interactions really do take place in our system, we characterised both precipitates **An** and **Bn** and SMPs by a range of analytical methods. FTIR spectra of all obtained SMPs showed no vibration bands from both NO_3^- groups and tetrabutylammonium cations (see ESI, Fig. S1–S6†). Similarly, elemental (CHN) analyses did not detect any nitrogen and carbon in the prepared materials. FTIR spectra and CHN analyses of **An** precipitates also demonstrated the elimination of Bu_4N^+ cations and NO_3^- ligands in the reactions of **1–3** with ammonia solution. Together these observations strongly support the assumption that **1–3** were fully hydrolysed during the Stöber process and/or had bonded to the silica matrix.

Hydrolysis of the starting cluster compounds *via* the simulated Stöber process was further confirmed by X-ray powder diffraction (XRPD) and thermogravimetric (TGA) analyses of precipitates **An** and **Bn**. The XRPD and TGA data for precipitates **An** and **Bn** are shown in ESI Fig. S7–S12.† The diffraction patterns of precipitates **A1** and **A2** have halo-like peaks with maxima at around 12.3 °C and 11.7 °C, respectively. The diffraction pattern of precipitate **A3** also showed a halo pattern and several broadened peaks with sharp apexes at 11.4 °C, 12.2 and 13.4 °C, which could come from a phase with a low crystallinity. We found that these peaks coincided with peaks in the theoretical diffraction pattern of the $[\{Mo_6I_8\}(H_2O)_2(OH)_4] \cdot 2H_2O$ (**6**·2H$_2$O) phase (CSD-number 429142). A mass loss was observed in the TGA curves of precipitates **An** in the 60 °C to 200 °C temperature range. The mass loss correlates well with removal of two crystallisation and two coordinated water

molecules from $[\{Mo_6X_8\}(H_2O)_2(OH)_4] \cdot 2H_2O$ with the formation of the earlier described cluster compounds $[\{Mo_6X_8\}(OH)_4]$.[36,37] Together these observations suggested that during the reaction of **1–3** with ammonia solution, we observe the formation of amorphous or lower crystallinity phases of $[\{Mo_6X_8\}(H_2O)_2(OH)_4] \cdot 2H_2O$ (precipitates **An**).

The XRPD of precipitates **Bn** showed increased crystallinity in comparison with precipitates **An**. We consider this to be attributed to chemical ageing of the solids. Namely, in the case of precipitate **B1**, we found two weak peaks at 10.5 °C and 11.7 °C that corresponded to a theoretical diffraction pattern of the crystalline phase $[\{Mo_6Cl_8\}(H_2O)_2(OH)_4] \cdot 12H_2O$ (**4**·12H$_2$O)[38] and a halo peak similar to precipitate **A1**. We also noticed some change in the colour of precipitate **B1** associated with the formation of molybdenum blue species. The TGA confirmed that precipitate **B1** still consisted mainly of amorphous **4**·2H$_2$O, while the content of **4**·12H$_2$O was below the detection limit of TGA.

The XRPD of precipitates **B2** showed coexistence of two phases: amorphous and crystalline. The profile of the amorphous phase corresponded to that found in **A2**, while sharp peaks were assigned to formation of the crystalline $[\{Mo_6Br_8\}(H_2O)_2(OH)_4] \cdot 12H_2O$ (**5**·12H$_2$O), which is isostructural to **4**·12H$_2$O. Indeed, we found several crystals on vial walls that were suitable for X-ray structural analysis. Single-crystal XRD clearly confirmed that the crystalline phase in precipitate **B2** corresponds to the proposed phase **5**·12H$_2$O (ESI, Table S1†). TGA of precipitate **B2** showed the loss of six water molecules, which means that it consisted of a mechanical mixture of 3 equivalents of **5**·2H$_2$O and 2 equivalents of **5**·12H$_2$O.

XRPD of precipitates **B3** showed a phase of high crystallinity with the pattern that coincided well with the theoretical diffraction pattern of **6**·2H$_2$O. TGA of precipitate **B3** confirmed the composition of **6**·2H$_2$O. On the walls of the vial, we also found few crystals. Surprisingly, the crystal structure was that of **6**·12H$_2$O, which has a different X-ray powder pattern. Taking into account the TGA and XRPD data, we assumed that most of the precipitate **B3** consisted of crystalline phase **6**·2H$_2$O with a minority admixture phase of crystalline **6**·12H$_2$O. Note that the content of the minor phase was below the detection limit of both TGA and XRPD methods.

Together the TGA and XRPD data of precipitates **An** and **Bn** suggest that hydrolysis of compounds **1–3** in ammonia solution occurs *via* the rapid formation of a metastable amorphous dihydrate phase. The ageing of these amorphous phases in aqueous media transforms them into more stable crystalline dodecahydrate or dihydrate phases.

In the powder diffraction patterns of neat SMPs and doped SMPs with $x \leq 0.1$ (Fig. S13–S15†), the typical halo patterns of SiO$_2$ glass at around 22 °C were observed.[43,44] The increased cluster content above $x = 0.1$ in the particles prepared from **2** and **3** led to both the weakening of the halo peak and the appearance of the new reflection peaks, which corresponded to those found in diffraction patterns of precipitates **A2** and **B3**, respectively. Namely, in the diffraction profile of 2^x@SiO$_2$, there was a broad halo peak around 11.7 °C, which narrowed with the increase in cluster loading of the SMPs. This peak was assigned
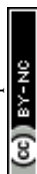
to the formation of amorphous aquahydroxo complex $5 \cdot 2H_2O$. In contrast to $2^x@SiO_2$, the diffraction patterns of $3^x@SiO_2$ ($x \geq 1$) featured reflections of crystalline phase $6 \cdot 2H_2O$ (Fig. 2).

The selected area electron diffraction patterns of samples $3^x@SiO_2$ (where $x = 0.05$, 0.5 and 5) further confirmed the amorphous state of the sample with low content of the cluster 3 (Fig. 3a), and the appearance of a crystalline phase in the samples with higher cluster content (Fig. 3b and c).

These observations signify that as metal-cluster complex loading increases above $x = 0.1$, the value z in the formula $[\{Mo_6X_8\}(H_2O)_{6-y-z}(OH)_y(OSi)_z]^{4-y-z}$ tends to 0.

^{29}Si CP MAS NMR of $3^{0.1}@SiO_2$, that is, the sample with the borderline content of the metal cluster complex, showed two noticeable changes in comparison to neat SiO_2 SMPs (Fig. 4): deshielding of the Q3-type signal (*i.e.*, Si–OH) by about 2 ppm and the increase in Q4/Q3 ratio. The change in the chemical environment of Si in the Q3-type can be explained by formation of hydrogen bonds between Si–OH and Mo–OH or Mo–OH$_2$, while increased intensity of the Q4 signal is likely the result of Si–O–Mo bond formation, which is in agreement with earlier ^{29}Si NMR data of doped silica materials.[26–28]

The UV/Vis diffuse reflectance spectra of SMPs (Fig. S16–S18†) displayed an enhanced optical absorption for cluster-doped particles in the visible region in comparison with neat SiO_2 particles, due to the presence of molybdenum cluster complexes. This is in the agreement with the cluster-loading dependent colour of the samples. Note that in the spectra of
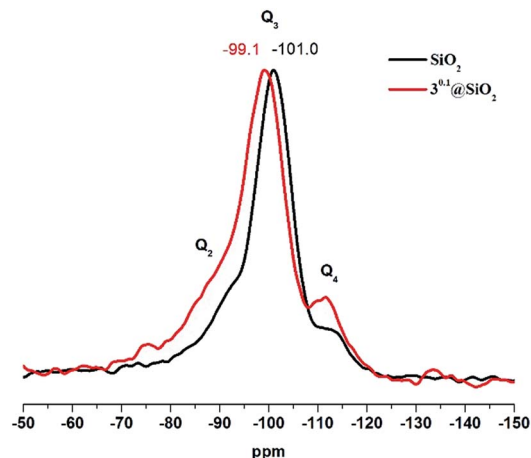

Fig. 4 ^{29}Si CP MAS NMR of neat SiO_2 and $3^{0.1}@SiO_2$ MPs.

both precipitate **B1** and $1^x@SiO_2$, where $x \geq 0.5$, absorption in the red region (>600 nm) was also observed. This absorption is due to the formation of molybdenum blue species,[45,46] as discussed above. The exact content (w/w) of molybdenum in SMPs was determined by ICP-AES analysis (see Fig. 5). The curves show the theoretical content calculated from the assumption that both cluster complexes **1–3** and TEOS are quantitatively hydrolysed to give $[\{Mo_6X_8\}(H_2O)_2(OH)_4] \cdot 2H_2O$ and SiO_2, respectively. The molybdenum contents in SMPs were found to be slightly lower than the theoretical ones. According to the TGA, this discrepancy is likely the result of 4–5% of water present in the samples (Fig. S19–S21†). The difference can also be the result of differences in hydrolysis kinetics of metal clusters and TEOS.

3.3 Materials morphology

Recently, Aubert *et al.* studied the influence of cluster complex $Cs_2[\{Mo_6Br_8\}Br_6]$ concentration in the reaction mixture on the size of obtained silica nanoparticles.[31] They demonstrated that particle diameter increased with rising cluster complex concentration in the reaction mixture. However, they used only
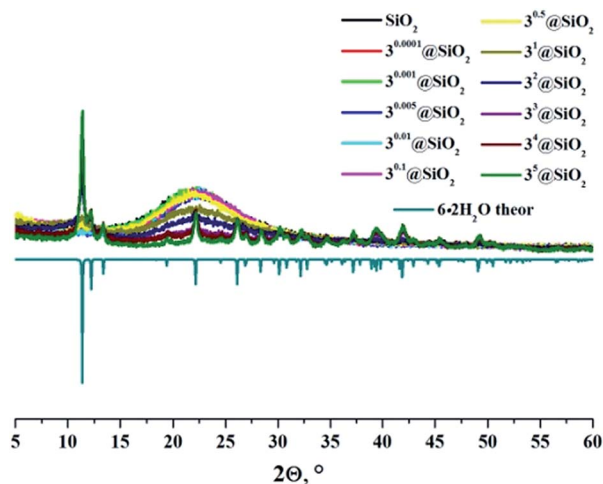

Fig. 2 X-ray powder diffraction patterns of neat and cluster-doped SMPs and theoretical diffraction pattern of $6 \cdot 2H_2O$.
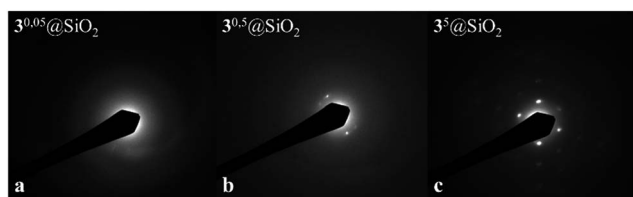

Fig. 3 Selected area electron diffraction patterns of samples $3^x@SiO_2$ where $x = 0.05$ (a), 0.5 (b) and 5 (c).
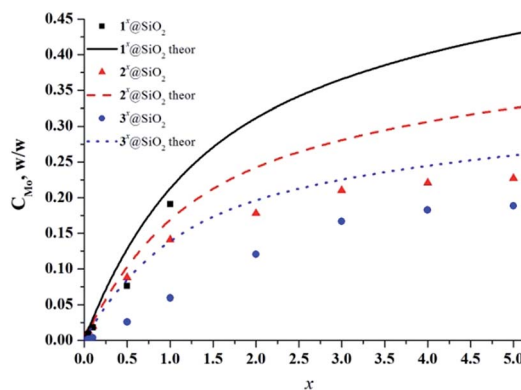

Fig. 5 Content of molybdenum in $n^x@SiO_2$ determined by ICP-AES analysis *versus* loading of metal cluster in SMPs (x).

a maximum of 20 mg of $Cs_2[\{Mo_6Br_8\}Br_6]$ per 1.5 mL of TEOS, which correlates with our sample $\mathbf{2^{0.05}@SiO_2}$. In our research we wanted to understand what happens to particle shapes and morphology, when the loading of molybdenum cluster complexes is increased even more, that is, when formation of the phases of $[\{Mo_6X_8\}(H_2O)_2(OH)_4]\cdot zH_2O$ is apparent.

The shapes and the morphology of all SMPs prepared here were characterised *via* TEM and the $\mathbf{3^x@SiO_2}$ series was also imaged by SEM (Fig. 6 and S22–S25†). The electron microscope images showed that both neat SiO_2 and SMPs with metal cluster content up to $x = 0.1$ possessed spherical shapes with nearly equal sizes of 500 nm (Fig. 6A). However, the increasing molybdenum cluster loadings in the SMPs above $x = 0.1$ resulted in distortion of particle spherical shapes (Fig. 6B) until complete disappearance of sphericity in $x \geq 0.5$ samples (Fig. 6C).

We also investigated the distribution of cluster complexes inside SMPs using electron energy-loss spectroscopy (EELS). Fig. S24† shows images of SMPs obtained *via* this technique, in which molybdenum atoms are depicted by red dots. The images demonstrate that molybdenum clusters are homogeneously distributed within the silica microbeads. Similarly, the confocal luminescence imaging of these SMPs (Fig. S26†) clearly showed that the emission from the molybdenum clusters was indeed uniformly distributed over all microparticles and they were localised within the microspheres.

3.4 Photophysical properties

Since the apical nitrato ligands of cluster complexes **1–3** are substituted during the Stöber process, it is important to determine how the immobilisation affects photophysical properties of the initial cluster complex. Indeed, our recent work showed that photoluminescence properties of compounds **1–3** changed strongly (especially in **3**), when they were incorporated into thiolated polystyrene microbeads. For example, incorporation of **3**, the compound with the highest photoluminescence quantum yield (PLQY) for molybdenum clusters in a fully inorganic environment,[5] led to slight broadening and red-shift of the luminescence spectrum and to an appreciable decrease of PLQY and emission lifetime values of the hybrid material. These changes were associated with the change in ligand environment around the $\{Mo_6X_8\}^{4+}$ cluster core (*i.e.*, substitution of

six NO_3^- ligands by thiol groups in the polymer matrix). In addition, earlier works on the incorporation of $Cs_2[\{Mo_6X_8\}X_6]$ and $(Bu_4N)_2[\{Mo_6I_8\}(CF_3CO_2)_6]$ into SiO_2 demonstrated that emission spectra of the cluster doped-silica materials were somewhat shifted relative to those of starting cluster complexes. The reported emission lifetimes for these materials were shorter than those for starting complexes, while PLQYs were not reported.[6,30,31]

Photoluminescence properties of SMPs were investigated on dry samples of $\mathbf{n^x@SiO_2}$. Emission spectra of the SMPs are shown in Fig. 7 and S27–S29,† while emission maximum wavelengths (λ_{em}), PLQYs (Φ_{em}) and lifetimes (τ_{em}) are summarised in Table S2.† Photophysical characteristics (λ_{em}, τ_{em}, and Φ_{em}) of **1–3** are summarised in Table S3† for comparison. The data show that the photoluminescence properties of $\mathbf{n^x@SiO_2}$ materials differ from those of starting compounds **1–3** (Fig. S30 and S31, Table S3†). Namely, the emission maxima showed bathochromic shifts of ∼60 nm for $\mathbf{1^x@SiO_2}$ and ∼85 nm for $\mathbf{2^x@SiO_2}$ and hypsochromic shift of ∼35 nm for $\mathbf{3^x@SiO_2}$ in comparison with corresponding starting complexes. Moreover, the increase in cluster loading of the SMPs independently on the cluster core composition led to the gradual bathochromic shift of the luminescence maxima (Table S3†). These shifts are due to changes in the apical ligand environment of the initial cluster complexes from $(NO_3)_6$ to $(H_2O)_{6-y-z}(OH)_y$-$(OSi)_z$, where z is likely to depend on the metal cluster to TEOS ratio in the reaction mixture (*i.e.*, the higher the ratio, the lower the z).

In addition to shifts in emission maxima, lifetimes and PLQYs were also significantly different. Similar to PLQY **3** *versus* that of **1** and **2**, the PLQYs of $\mathbf{3^x@SiO_2}$ materials were significantly higher (up to 0.09) than that for any of the $\mathbf{1^x@SiO_2}$ and $\mathbf{2^x@SiO_2}$ SMPs (<0.01).

Detailed study of photophysical properties for a large series of $\mathbf{3^x@SiO_2}$ showed that the PLQYs appreciably decreased with an excessive increase in cluster loading of silica (Table S4†). Specifically, the materials $\mathbf{3^x@SiO_2}$, where x was in the 0.0002–0.002 range, showed the highest PLQY values up to 0.09, while
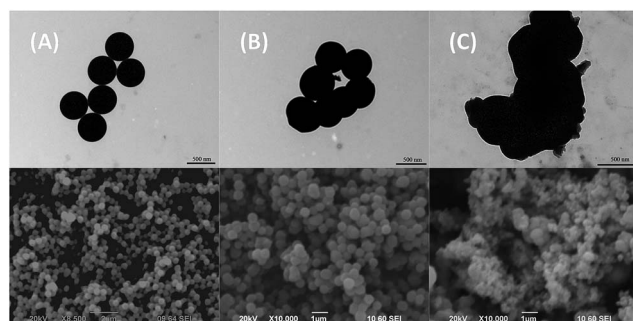

Fig. 6 TEM and SEM images of $\mathbf{3^x@SiO_2}$ SMPs. (A) $x = 0.001$; (B) $x = 0.1$; (C) $x = 1$.
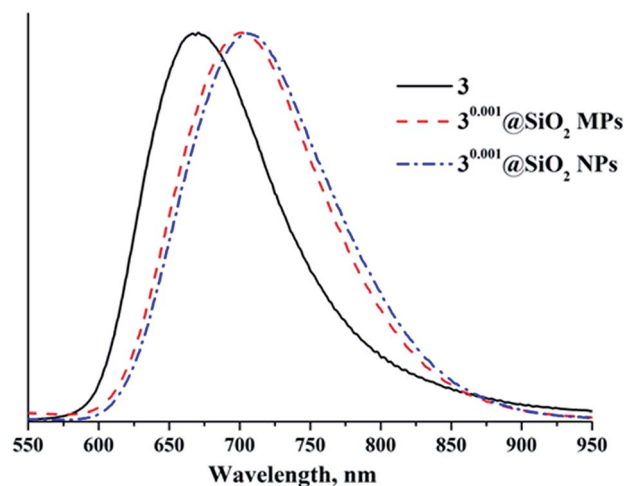

Fig. 7 Emission spectra of cluster **3** and $\mathbf{3^{0.001}@SiO_2}$ SMPs and SNPs.

further increase in cluster content led to the smooth decrease in PLQYs down to 0.01. Presumably, such a decrease in PLQYs is associated with formation of $6 \cdot 2H_2O$ crystallites in $3^x@SiO_2$, when $x \geq 0.002$. It is worth noting that PLQYs of $3^x@SiO_2$, where $x < 0.0002$, also led to the decrease in PLQYs, probably due to insignificant quantities of cluster complexes.

To evaluate the influence of aquahydroxo complex formation in SMPs on the materials' photophysical characteristics, we also examined luminescence properties on precipitates **A1–A3** and **B2**. Precipitates **A1**, **A2** and **B2** showed typical behaviour for octahedral molybdenum cluster complexes with broad emission bands, while precipitate **A3** did not exhibit any luminescence at all (Fig. S32 and S33, Table S3†). The maximum wavelength emission of precipitates **A1** and **B1** were found to be ~745 nm, while the PLQY was less than 0.01. Unexpectedly, we observed that the emission from precipitates **A2** and **B2** was slightly brighter than that from **A1** and **B1** or **A3** and **B3**. Notably, the emission spectra profiles of precipitates **A2** and **B2** were somewhat different with maximum wavelengths of ~715 and ~705 nm and PLQYs of less than 0.01 and 0.02, respectively. These discrepancies between two chemically similar solids can be explained by either the influence of crystallisation water molecules on luminescence properties or by the effect of solids structure (amorphous $5 \cdot 2H_2O$ vs. mixture of amorphous $5 \cdot 2H_2O$ and crystalline $5 \cdot 12H_2O$).

In summary, the poor emission of **1** and **2** and related aquahydroxo complexes resulted in SMP materials with very weak emissions, while the absence of photoluminescence in $6 \cdot 2H_2O$ (precipitates **A3** and **B3**) explains well the decrease in both PLQYs and lifetimes for $3^x@SiO_2$, when $x \geq 0.002$. There is, however, a "sweet spot" in $3^x@SiO_2$ series of SMPs: materials with x in the range 0.0002–0.002 have quite an intensive emission.

3.5 Singlet-oxygen generation

As previously mentioned, the luminescence from hexamolybdenum cluster complexes **1–3** is efficiently quenched by oxygen. The emission quenching is due to energy transfer from the excited cluster complex to triplet oxygen ($^3O_2$), which results in generation of $^1O_2$.[11,12] The organic compound 2,3-diphenyl-*para*-dioxene is well established as a singlet-oxygen trap (Scheme S1†), since it is easily oxidised by singlet oxygen.[47,48] Fig. S34† demonstrates ^1H NMR spectra of acetone solutions of 2,3-diphenyl-*para*-dioxene and the cluster complexes **1–3** after 3 h of radiation by light with $\lambda \geq 400$ nm. The appearance of a singlet peak at 4.72 ppm that corresponds to the methylene protons of ethylene glycol dibenzoate (*i.e.*, the product of oxidation of 2,3-diphenyl-*para*-dioxene by $^1O_2$) indicates the generation of singlet oxygen during the photoirradiation of solutions containing cluster complexes. The resultant concentration of ethylene glycol dibenzoate and calculated conversion of 2,3-diphenyl-*para*-dioxene after photoirradiation are given in Table S5.† According to the data, complex **3** was the most powerful photosensitiser. As discussed above, it is also the most efficient luminophore. Interestingly, the oxidation of 2,3-diphenyl-*para*-dioxene in the presence of **1** and **2** was also efficient, despite weak luminescence properties of these

complexes. Indeed, conversion of the singlet-oxygen trap in the presence of **1** and **2** was of the same order of magnitude as in the presence of **3**.

Photosensitizing ability of cluster-doped SMPs was also investigated. Fig. 8 shows graphs of 2,3-diphenyl-*para*-dioxene conversion *versus* illumination time in the presence of nine samples of various SMPs. According to the data obtained, the increase in illumination time led to the gradual increase of singlet-oxygen trap conversion. There was also a tendency for SMPs with higher loadings of the cluster complex ($x = 0.05$ and 0.1) to show a slight increase in conversion of the trap molecule.

3.6 Influence of particle size on photophysical properties

To obtain photoluminescent silica nanoparticles (SNPs) of composition $3^x@SiO_2$ (where $x = 0, 0.001, 0.005, 0.01, 0.05, 0.1$) and monodisperse size distribution, the Stöber process was carried out in water-in-oil emulsion in the presence of compound **3** using a slightly modified synthetic protocol from Aubert *et al.*[31]

FTIR spectra and elemental analyses of the obtained SNPs confirmed both successful displacement during reactions of all apical nitrato ligands and Bu_4N^+ cations in the initial cluster complex **3** and successful removal of all Brij®L4 surfactant during the washing of SNPs. TEM images showed that all SNPs had a perfectly spherical shape and increase in particle size from 55 nm to 65 nm with the increase of x (Fig. 9). In a similar manner as for SMPs, the set of analytical techniques (XRPD, FTIR, UV/Vis diffuse reflectance spectroscopies and elemental analysis) unambiguously confirmed the presence of the molybdenum cluster complex in the SNPs and the similar chemical environment of the molybdenum metal cluster in both SMPs and SNPs.

To evaluate the impact of particle size on the materials' luminescence properties, we also determined photophysical characteristics of $3^x@SiO_2$ SNPs (Fig. 7 and S35, Table S3†). It was found that photoluminescence properties of the SNPs, when $x \leq 0.005$, are similar to those of SMPs, while an increase in cluster loading above this value led to more significant reductions of both PLQY and photoluminescence lifetimes in the case of SNPs than for SMPs. This is likely to be connected
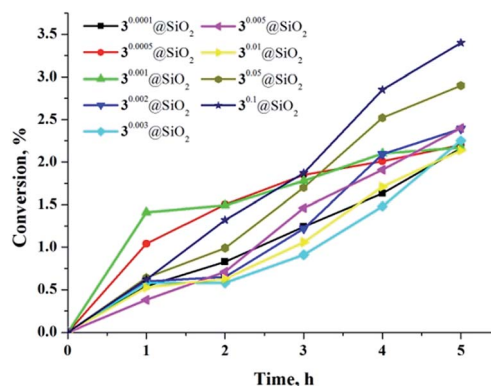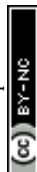

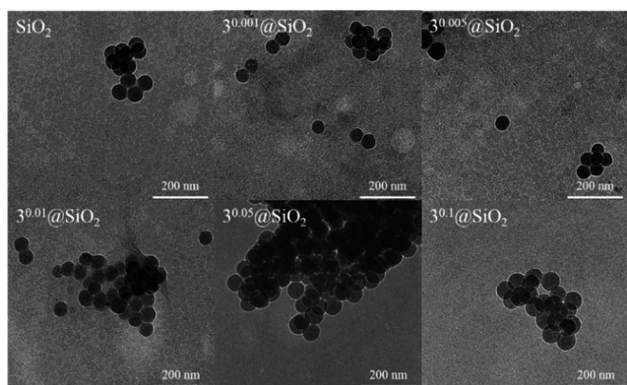**Fig. 8** Conversion of 2,3-diphenyl-*para*-dioxene in presence of various SMPs *versus* illumination time.

Fig. 9 TEM image of neat SiO_2 and 3^x@SiO_2 NPs.

with the higher degree of hydrolysis in the molybdenum cluster precursor for SNPs, due to longer reaction time. Indeed, according to ICP-AES, the actual content of molybdenum in SNPs, when $x \geq 0.01$, is higher than that in corresponding SMPs (Table 1).

When we compared singlet-oxygen trap conversions in the presence of SNPs (3^x@SiO_2, x = 0.001, 0.005 and 0.01) with conversion in the presence of similar SMPs, we observed that not only did SNPs generate singlet oxygen, but also the efficiency of $^1O_2$ generation by SNPs was approximately fourfold greater than by SMPs (Fig. 10). We believe that the reason for

Table 1   Actual content of metal cluster in particles n^x@SiO_2 determined by ICP-AES analysis; SMPs versus SNPs

Sample	C_{Mo}, w/w for SMPs[a]	C_{Mo}, w/w for SNPs[a]
$3^{0.001}$@SiO_2	0.00016	0.00016
$3^{0.005}$@SiO_2	0.00056	0.00044
$3^{0.01}$@SiO_2	0.00085	0.0011
$3^{0.05}$@SiO_2	0.0021	0.0049
$3^{0.1}$@SiO_2	0.0040	0.0072

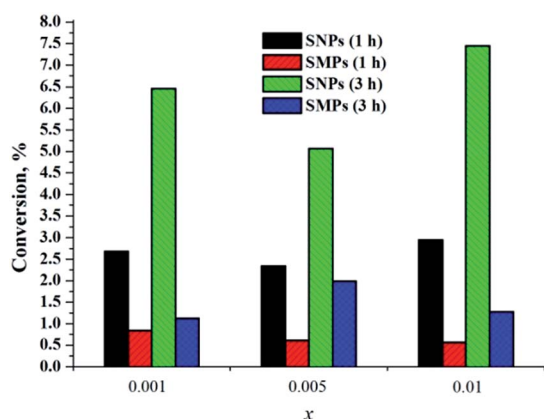[a] Relative error of a single determination does not exceed 10%.

Fig. 10   Singlet oxygen generation by SMPs and SNPs 3^x@SiO_2 (x = 0.001, 0.005 and 0.01) after 1 h and 3 h.

enhanced efficiency of singlet oxygen generation by SNPs is due to higher surface area of the material, which critically affects the rate of interaction of $^3O_2$ with the cluster-doped silica. Indeed, the specific surface area of SMPs obtained by BET measurements was ~60 m^2 g^{-1}, while it was ~280 m^2 g^{-1} for SNPs, that is, nearly 5 times higher. The nitrogen sorption isotherms are shown in Fig. S36.†

4.   Conclusions

In this work we have thoroughly studied the hybrid materials that are realised in the Stöber process in the presence of hexamolybdenum cluster complexes $(Bu_4N)_2[\{Mo_6X_8\}(NO_3)_6]$ (X = Cl, Br, or I). We have shown that photoluminescence properties of resultant materials depend not only on composition of the cluster core $\{Mo_6X_8\}^{4+}$, but also on loading of the metal cluster complex in the material. This is due to two processes that occur during material formation: substitution of nitrato ligands by silanol groups and hydrolysis of cluster complexes, which leads to formation of poorly luminescent compounds $[\{Mo_6X_8\}(H_2O)_2(OH)_4]\cdot 2H_2O$. Specifically, we have established that SMPs with composition 3^x@SiO_2, where x lies in the 0.0002–0.002 range, show the highest photoluminescence quantum yields. Formation of the corresponding aqua-hydroxo complex phase has also an effect on silica particle morphology, i.e., the spherical shape of the particles is significantly distorted when $x \geq 0.5$.

Comparison of microparticle photophysical properties with those of nanoparticles showed that size does not influence emission spectral shape, while luminescence quantum yields and SMP lifetimes are slightly higher and longer, respectively, than those from corresponding SNPs. This is due to greater surface area of the SNPs, which results in more significant quenching of photoluminescence by oxygen. This assumption is further confirmed by the higher singlet oxygen generation efficiency of SNPs in comparison with those of SMPs.

We suggest that photoluminescent particles of composition 3^x@SiO_2, where x is in the 0.0002–0.002 range are highly promising materials for applications such as agents for bioimaging, biolabeling or PDT. Indeed, these cluster-doped SMPs show appreciably bright photoluminescence within the optical tissue window and the ability to generate singlet oxygen. The relevant biological properties of these materials are currently under investigation.

Acknowledgements

Notes and references

1 S. Cordier, F. Grasset, Y. Molard, M. Amela-Cortes, R. Boukherroub, S. Ravaine, M. Mortier, N. Ohashi, N. Saito and H. Haneda, *J. Inorg. Organomet. Polym. Mater.*, 2015, **25**, 189–204.

2 M. N. Sokolov, M. A. Mihailov, E. V. Peresypkina, K. A. Brylev, N. Kitamura and V. P. Fedin, *Dalton Trans.*, 2011, **40**, 6375–6377.

3 M. N. Sokolov, M. A. Mikhailov, K. A. Brylev, A. V. Virovets, C. Vicent, N. B. Kompankov, N. Kitamura and V. P. Fedin, *Inorg. Chem.*, 2013, **52**, 12477–12481.

4 M. N. Sokolov, M. A. Mikhailov, A. V. Virovets, K. A. Brylev, R. A. Bredikhin, A. M. Maksimov, V. E. Platonov and V. P. Fedin, *Russ. Chem. Bull.*, 2013, **62**, 1764–1767.

5 O. A. Efremova, M. A. Shestopalov, N. A. Chirtsova, A. I. Smolentsev, Y. V. Mironov, N. Kitamura, K. A. Brylev and A. J. Sutherland, *Dalton Trans.*, 2014, **43**, 6021–6025.

6 K. Kirakci, P. Kubat, M. Dusek, K. Fejfarova, V. Sicha, J. Mosinger and K. Lang, *Eur. J. Inorg. Chem.*, 2012, 3107–3111.

7 K. Kirakci, P. Kubat, J. Langmaier, T. Polivka, M. Fuciman, K. Fejfarova and K. Lang, *Dalton Trans.*, 2013, **42**, 7224–7232.

8 K. Kirakci, K. Fejfarova, M. Kucerakova and K. Lang, *Eur. J. Inorg. Chem.*, 2014, **2014**, 2331–2336.

9 K. Kirakci, V. Sicha, J. Holub, P. Kubat and K. Lang, *Inorg. Chem.*, 2014, **53**, 13012–13018.

10 M. A. Mikhailov, K. A. Brylev, A. V. Virovets, M. R. Gallyamov, I. Novozhilov and M. N. Sokolov, *New J. Chem.*, 2016, **40**, 1162–1168.

11 J. A. Jackson, M. D. Newsham, C. Worsham and D. G. Nocera, *Chem. Mater.*, 1996, **8**, 558–564.

12 J. A. Jackson, C. Turro, M. D. Newsham and D. G. Nocera, *J. Phys. Chem.*, 1990, **94**, 4500–4507.

13 K. Kirakci, P. Kubát, V. Kučeráková, V. Šícha, H. Gbelcová, P. Lovecká, P. Grznárová, T. Ruml and K. Lang, *Inorg. Chim. Acta*, 2016, **441**, 42–49.

14 K. Kirakci, P. Kubát, K. Fejfarova, J. Martincik, M. Nikl and K. Lang, *Inorg. Chem.*, 2016, **55**, 803–809.

15 M. Amela-Cortes, A. Garreau, S. Cordier, E. Faulques, J. L. Duvail and Y. Molard, *J. Mater. Chem. C*, 2014, **2**, 1545–1552.

16 J. Elistratova, V. Burilov, A. Mustafina, M. Mikhailov, M. Sokolov, V. Fedin and A. Konovalov, *Polymer*, 2015, **72**, 98–103.

17 A. Garreau, F. Massuyeau, S. Cordier, Y. Molard, E. Gautron, P. Bertoncini, E. Faulques, J. Wery, B. Humbrt, A. Bulou and J.-L. Duvail, *ACS Nano*, 2013, **7**, 2977–2987.

18 Y. Molard, C. Labbé, J. Cardin and S. Cordier, *Adv. Funct. Mater.*, 2013, **23**, 4821–4824.

19 O. A. Efremova, K. A. Brylev, Y. A. Vorotnikov, L. Vejsadová, M. A. Shestopalov, G. F. Chimonides, P. D. Topham, N. Kitamura and A. J. Sutherland, *J. Mater. Chem. C*, 2016, **4**, 497–503.

20 N. A. Vorotnikova, O. A. Efremova, A. R. Tsygankova, K. A. Brylev, M. V. Edeleva, O. G. Kurskaya, A. J. Sutherland, A. M. Shestopalov, Y. V. Mironov and M. A. Shestopalov, *Polym. Adv. Technol.*, 2016, DOI: 10.1002/pat.3749.

21 D. Tarn, C. E. Ashley, M. Xue, E. C. Carnes, J. I. Zink and C. J. Brinker, *Acc. Chem. Res.*, 2013, **46**, 792–801.

22 J. Kim, Y. Piao and T. Hyeon, *Chem. Soc. Rev.*, 2009, **38**, 372–390.

23 S. W. Bae, W. H. Tan and J. I. Hong, *Chem. Commun.*, 2012, **48**, 2270–2282.

24 W. Arap, R. Pasqualini, M. Montalti, L. Petrizza, L. Prodi, E. Rampazzo, N. Zaccheroni and S. Marchio, *Curr. Med. Chem.*, 2013, **20**, 2195–2211.

25 S. Chinnathambi, S. Chen, S. Ganesan and N. Hanagata, *Adv. Healthcare Mater.*, 2014, **3**, 10–29.

26 C. D. Nunes, A. A. Valente, M. Pillinger, J. Rocha and I. S. Gonçalves, *Chem.–Eur. J.*, 2003, **9**, 4380–4390.

27 L. Hu, S. Ji, T. Xiao, C. Guo, P. Wu and P. Nie, *J. Phys. Chem. B*, 2007, **111**, 3599–3608.

28 R. B. Watson and U. S. Ozkan, *J. Phys. Chem. B*, 2002, **106**, 6930–6941.

29 M. Y. Kirillin, E. A. Sergeeva, P. D. Agrba, A. D. Krainov, A. A. Ezhov, D. V. Shuleiko, P. K. Kashkarov and S. V. Zabotnov, *Laser Phys.*, 2015, **25**, 075604.

30 F. Grasset, F. Dorson, S. Cordier, Y. Molard, C. Perrin, A. M. Marie, T. Sasaki, H. Haneda, Y. Bando and M. Mortier, *Adv. Mater.*, 2008, **20**, 143–148.

31 T. Aubert, F. Cabello-Hurtado, M. A. Esnault, C. Neaime, D. Lebret-Chauvel, S. Jeanne, P. Pellen, C. Roiland, L. Le Polles, N. Saito, K. Kimoto, H. Haneda, N. Ohashi, F. Grasset and S. Cordier, *J. Phys. Chem. C*, 2013, **117**, 20154–20163.

32 J.-F. Dechézelles, T. Aubert, F. Grasset, S. Cordier, C. Barthou, C. Schwob, A. Maître, R. A. Vallée, H. Cramail and S. Ravaine, *Phys. Chem. Chem. Phys.*, 2010, **12**, 11993–11999.

33 P. Braack, M. K. Simsek and W. Preetz, *Z. Anorg. Allg. Chem.*, 1998, **624**, 375–380.

34 R. K. Summerbell and D. R. Berger, *J. Am. Chem. Soc.*, 1959, **81**, 633–639.

35 J. C. Sheldon, *Nature*, 1959, **184**, 1210–1213.

36 J. C. Sheldon, *J. Chem. Soc.*, 1962, 410–415.

37 J. C. Sheldon, *J. Chem. Soc.*, 1960, 1007–1014.

38 C. Brosset, *Ark. Kemi, Mineral. Geol.*, 1945, **20**, 1–16.

39 J. C. Sheldon, *Chem. Ind.*, 1961, 323.

40 J. C. Sheldon, *J. Chem. Soc.*, 1963, 4183–4186.

41 J. C. Sheldon, *J. Chem. Soc.*, 1964, 1287–1291.

42 L. M. Robinson, H. Lu, J. T. Hupp and D. F. Shriver, *Chem. Mater.*, 1995, **7**, 43–49.

43 B. P. Zhang, H. Masumoto, Y. Someno and T. Goto, *Mater. Trans.*, 2003, **44**, 215–219.

44 X. J. Zhang and H. G. Zheng, *Bull. Mater. Sci.*, 2008, **31**, 787–790.

45 B. Botar, A. Ellern and P. Kogerler, *Dalton Trans.*, 2012, **41**, 8951–8959.

46 J. Jonca, C. Barus, W. Giraud, D. Thouron, V. Garcon and M. Comtat, *Int. J. Electrochem. Sci.*, 2012, **7**, 7325–7348.

47 L. Gao, M. A. Peay and T. G. Gray, *Chem. Mater.*, 2010, **22**, 6240–6245.

48 M. A. Shestopalov, K. E. Zubareva, O. P. Khripko, Y. I. Khripko, A. O. Solovieva, N. V. Kuratieva, Y. V. Mironov, N. Kitamura, V. E. Fedorov and K. A. Brylev, *Inorg. Chem.*, 2014, **53**, 9006–9013.